SENSITIVITY OF SEPARATION INDICATORS IN SPACECRAFT FORMATION COLLISION RISK ANALYSIS

Ulises E. Núñez Garzón,[*] and E. Glenn Lightsey[†]

The 99.73% minimum distance, denoted as $\rho_{3\sigma}$, is the 0.27%-percentile in the distribution of the norm of the instantaneous relative position between two agents. Previously, $\rho_{3\sigma}$ has been proposed as a probabilistic collision risk boundary for spacecraft formation flight under the assumption of Clohessy-Wiltshire (CW) relative orbital dynamics. In this case, agents with lesser separation than $\rho_{3\sigma}$ have an instantaneous collision probability higher than 0.27%. This work validates the foregoing interpretation of $\rho_{3\sigma}$ by showing that small changes to the target probability of $\rho_{3\sigma}$ also result in small changes to $\rho_{3\sigma}$ itself.

INTRODUCTION

Spacecraft formation flying (SFF) is defined as a "set of more than one spacecraft whose dynamic states are coupled through a common control law".[1] Spacecraft formations are attractive from a space mission design perspective. In particular, SFF can enable missions with increased system robustness, as deterioration or failure of an agent in a spacecraft formation may only cause performance degradation in the mission, rather than causing the end of the mission.[2] Conversely, spacecraft formation missions may also have longer lifetimes due to the ability to replace failed agents or add new ones. This adds new options to space mission architectures beyond those available to traditional, monolithic spacecraft missions.[3] Additionally, missions that implement SFF have an opportunity for enhanced system flexibility through improved "adaptability, scalability, evolvability, and maintainability".[4] Spacecraft formations can also enable high precision scientific missions by distributing a formation over regions larger than those spanned by large, monolithic spacecraft and by using sensor fusion.[5] Doing so has a plethora of applications, such as gravimetry,[6] weather forecasting and climate monitoring,[7] exoplanet detection,[8] gravitational wave detection,[9] and more.

Spacecraft formations are intended to exhibit safe and continued operation, but this goal might be jeopardized by the ever-present risk of collision events, which could occur among agents in a formation or between any such agent and debris that are external to a formation.[10, 11] Since orbit navigation, dynamic modeling, and actuation errors, even if reducible, cannot be fully eliminated, some level of inter-spacecraft drift is inherent to spacecraft formations;[2] hence, it is always possible that such drifting might cause internal collision events. Approaches to SFF collision avoidance (COLA) can be broadly classified into two groups: passive and active.[12, 13] Passive SFF COLA methods focus on designing and keeping orbits that are passively safe (approximately), without directly addressing internal collision risk in an ongoing basis.[14–16] Conversely, active SFF COLA methods propose conducting internal collision risk quantification and assessment on a recurring basis, as well as planning and executing corrective actions when necessary.

Active SFF COLA methods are characterized by their collision risk indicators, which are used to quantify collision risk; these indicators are employed in developing threshold criteria through which it can be decided whether collision risk warrants corrective maneuvers. The first indicator type, distance-based, employs some statistical description of the physical separation between two agents as measured by, for example, the

---

[*]Graduate Research Assistant, Space Systems Design Lab, Guggenheim School of Aerospace Engineering, Georgia Institute of Technology, 620 Cherry St NW, Atlanta, GA 30332.

[†]Professor, Space Systems Design Lab, Guggenheim School of Aerospace Engineering, Georgia Institute of Technology, 620 Cherry St NW, Atlanta, GA 30332.

Euclidean distance or Cartesian components of relative position.[17–20] The second indicator type, probability-based, quantifies collision risk as the probability measure of the relative position over a region in which the collision event is understood to occur.[10, 12, 13, 21–23] Generally, collision risk is mitigated by setting constraints in an optimal control problem in terms of these indicators. Because distance-based and probability-based indicators have distinct physical interpretations, active SFF COLA methods are philosophically and practically distinct depending on the choice of collision risk indicator. For an extended discussion on distance-based and probability-based collision risk indicators and their relationship, the reader is encouraged to refer to the work of Núñez Garzón et al.[12, 13]

For an individual agent, its hard-body radius (HBR) is a safety parameter that describes the minimum safe distance from its center of mass to any objects outside itself. Consequently, the joint hard-body radius for two agents, which is the sum of their individual hard-body radii, may be understood as a minimum safe separation distance between such agents. Hence, a collision between two agents may be defined to occur when the distance between their centers of mass is less than their joint HBR. Then, the kinematic probability of collision (KPC) between two agents is the probability of this instantaneous collision event, given a stochastic description of the relative geometry between such agents.

If $p_{3\sigma}$ is defined as a constant with an approximate value of 0.27%, then the 99.73% minimum distance value, also known as $\rho_{3\sigma}$, is the distance away from the origin (of the frame of the relative position between two agents) such that $100(1 - p_{3\sigma})$ percent of randomly drawn points (according to the relative position distribution) have a distance from the origin greater than $\rho_{3\sigma}$. In the context of Clohessy-Wiltshire (CW) relative orbital dynamics,[24, 25] $\rho_{3\sigma}$ has been proposed as an inter-agent separation indicator with two benefits.[12, 13] First, through its definition, $\rho_{3\sigma}$ has the following probabilistic risk interpretation: $\rho_{3\sigma}$ is the joint HBR such that the corresponding KPC is equal to $p_{3\sigma}$. Second, with a fixed joint HBR, the corresponding KPC time-waveform has a correlation relationship with the $\rho_{3\sigma}$ time-waveform such that, roughly, local minima of KPC correspond with local maxima of $\rho_{3\sigma}$, and vice versa. That is, roughly, $\rho_{3\sigma}$ indicates closest inter-agent distance in the same conditions that the KPC indicates highest collision risk, and $\rho_{3\sigma}$ indicates furthest inter-agent distance while the KPC indicates lowest risk. Therefore, $\rho_{3\sigma}$ and the KPC are correlated to each other in a way that is consistent with intuition.

In the following way, $\rho_{3\sigma}$ can be interpreted as a probabilistic risk boundary: if the joint HBR for two agents were equal to $\rho_{3\sigma}$, then the instantaneous probability of collision between the agents would be equal to $p_{3\sigma}$. Hence, if the true joint HBR is less than $\rho_{3\sigma}$, the instantaneous collision probability is less than $p_{3\sigma}$; conversely, if the true joint HBR is greater than $\rho_{3\sigma}$, the instantaneous collision probability is greater than $p_{3\sigma}$. As a result, $\rho_{3\sigma}$ conceptually bridges the gap between probabilistic and distance-based approaches to collision risk quantification.

In order to validate this interpretation of $\rho_{3\sigma}$, it is important to understand the effects on $\rho_{3\sigma}$ caused by variations in its target probability, i.e. the value of the probability measure to be achieved at the $\rho_{3\sigma}$ value, which should be equal to $p_{3\sigma}$ by definition. However, because of errors inherent to numerical methods, it is expected that there would be a discrepancy between the prescribed $p_{3\sigma}$ value and the computed radial probability measure at the true $\rho_{3\sigma}$. Such discrepancies may affect both the meaning of $\rho_{3\sigma}$ and its computation. First, finding a $\rho_{3\sigma}$ candidate that achieves a target probability that approximates (but is not exactly equal to) $p_{3\sigma}$ is equivalent to solving for $\rho_{3\sigma}$ with a target probability different from $p_{3\sigma}$. Hence, if small variations in target probability result in changes to $\rho_{3\sigma}$ that are small compared to the magnitude of $\rho_{3\sigma}$, then it makes sense to assert that a collision risk of approximately $p_{3\sigma}$ is incurred when the inter-agent keep-out distance is approximately $\rho_{3\sigma}$. Second, if small changes in target probability cause small changes in $\rho_{3\sigma}$, the outcome of an estimator of $\rho_{3\sigma}$ could be trusted to hold the same interpretation as the true $\rho_{3\sigma}$. Therefore, the goal of this work is to examine the sensitivity of $\rho_{3\sigma}$ to small variations in its target probability. If such an investigation validates the foregoing interpretation of $\rho_{3\sigma}$, especially over extended propagation horizons, it would justify application of the $\rho_{3\sigma}$ construct in spacecraft formation collision risk analysis.

This work is organized as follows. In the Background section, the notation and terminology employed is expounded, and the topological notions of collision events and collision probability are formulated. In the Theory section, the norm of the relative position is characterized as a random variable. This allows

for the computation of radial probability measures, as well as for the interpretation of $\rho_{3\sigma}$ as a quantile of the distribution of the norm of the relative position – all of which lays the foundation for the sensitivity analysis of $\rho_{3\sigma}$. The Methodology section details the precise techniques employed for numerical and sample computation of $\rho_{3\sigma}$, which, in turn, are applied to computing the sensitivity of $\rho_{3\sigma}$. In the Results and Conclusion sections, the outcome of this analysis is summarized, and the implications are discussed.

BACKGROUND

This section introduces some preliminary concepts that are used in the following analysis. First, the notation used in this work is established. Next, the formal, topological notions of collision events and collision probability are presented. Finally, simulation cases with the assumption of Clohessy-Wiltshire (CW) relative orbital dynamics and geometry are defined.

Notation

Vectors are underlined, while matrices and functions are not. Although boldface is reserved for multi-dimensional variables (i.e. vectors and matrices), sometimes boldfacing such variables may be avoided for clarity. Let $\underline{\mathbf{X}} \in \mathbb{R}^{n_{\underline{\mathbf{X}}}}$ and $\underline{\mathbf{R}} \in \mathbb{R}^{d_{\underline{\mathbf{R}}}}$ denote a dynamic state and position state, respectively. The dimensions of $\underline{\mathbf{X}}$ and $\underline{\mathbf{R}}$ are denoted by $n_{\underline{\mathbf{X}}}$ and $d_{\underline{\mathbf{R}}}$, respectively. (Note: $d_{\underline{\mathbf{R}}} \in \{1, 2, 3\}$.) When used with the subscript i, $\underline{\mathbf{X}}_i$ and $\underline{\mathbf{R}}_i$ denote the dynamic state and position of agent i, respectively. It is understood that $\underline{\mathbf{R}}_i$ specifically refers to the position of the center of mass of agent i. When used with a composite subscript such as "i-j", $\underline{\mathbf{X}}_{i,j}$ and $\underline{\mathbf{R}}_{i,j}$ denote the dynamic state and position of agent i relative to agent j, respectively, i.e. $\underline{\mathbf{X}}_{i,j} \doteq \underline{\mathbf{X}}_i - \underline{\mathbf{X}}_j$ and $\underline{\mathbf{R}}_{i,j} \doteq \underline{\mathbf{R}}_i - \underline{\mathbf{R}}_j$. (For a mathematical object a and expressions LHS and RHS, the statement "$a \doteq \mathrm{RHS}$" denotes that a is defined via the expression RHS, whereas the statement "$\mathrm{LHS} =: a$" indicates that the expression LHS is equal to a by definition.)

When written in uppercase, $\underline{\mathbf{X}}$ and $\underline{\mathbf{R}}$ denote an uncertain dynamic state and uncertain position, respectively, i.e. a dynamic state $\underline{\mathbf{X}}(t)$ and position $\underline{\mathbf{R}}(t)$ are random variables (RVs) for any time t. Conversely, when written in lowercase, $\underline{\mathbf{x}}$ and $\underline{\mathbf{r}}$ denote specific, deterministic "instances" or values that $\underline{\mathbf{X}}$ and $\underline{\mathbf{R}}$ may take on, respectively. When inside a square bracket and with a subscript outside of such bracket, $[\underline{\mathbf{R}}]_{\mathcal{J}} \in \mathbb{R}^{d_{\underline{\mathbf{R}}}}$ denotes that $\underline{\mathbf{R}} \in \mathbb{R}^{d_{\underline{\mathbf{R}}}}$ is expressed in the coordinates of a reference frame $\mathcal{J}$; similarly, $[b]_{\mathcal{J}} \in \mathbb{R}$ denotes the bth component of $\underline{\mathbf{R}}$ in the $\mathcal{J}$-frame ($b \in \{x, y, z\}$).

It is assumed that $\underline{\mathbf{X}}(t)$ and $\underline{\mathbf{R}}(t)$ are absolutely continuous for any time t; that is, probability measures of $\underline{\mathbf{X}}(t)$ and $\underline{\mathbf{R}}(t)$ are zero-valued on sets of zero measure in their respective sample spaces.[26] Consequently, probability density functions (pdfs) for $\underline{\mathbf{X}}(t)$ and $\underline{\mathbf{R}}(t)$ exist almost everywhere (a.e.) in their respective sample spaces, and probability measures on $\underline{\mathbf{X}}(t)$ and $\underline{\mathbf{R}}(t)$ can be computed as integrals of their pdfs.[27] Additionally, only instantaneous events are considered in this work; that is, only events that pertain to the distribution of $\underline{\mathbf{X}}(t)$ and $\underline{\mathbf{R}}(t)$ at a single time t are considered. Hence, the dependence of the distribution of $\underline{\mathbf{X}}(t)$ and $\underline{\mathbf{R}}(t)$ on t is often implicit. Finally, the cumulative distribution function (cdf) of a univariate, real-valued random variable X is denoted by $\mathrm{cdf}_X(\cdot)$.

Definition of a collision event

This subsection mirrors the topological notions of collision as previously presented by Núñez Garzón et al.[12,13,21] A collision event (between two agents) occurs whenever their respective physical, nonempty "volumes" in $d_{\underline{\mathbf{R}}}$-dimensional space have a nonempty intersection, i.e. a collision occurs when agents bodies occupy portions of the same volume of space at the same time.

Definition 1 (n-ball and $(n-1)$-sphere[28,29]). The n-ball and $(n-1)$-sphere of radius r (centered at $\underline{x} \in \mathbb{R}^n$), denoted by $\mathbb{B}_r^n(\underline{x})$ and $\mathbb{S}_r^{(n-1)}(\underline{x})$, respectively, are defined as the sets

$$\mathbb{B}_r^n(\underline{x}) \doteq \left\{ \underline{y} \in \mathbb{R}^n : \left\| \underline{x} - \underline{y} \right\| < r, r > 0 \right\} \tag{1}$$

$$\mathbb{S}_r^{(n-1)}(\underline{x}) \doteq \left\{ \underline{y} \in \mathbb{R}^n : \left\| \underline{x} - \underline{y} \right\| = r, r > 0 \right\} \tag{2}$$

Note: when the dimension of elements in $\mathbb{B}_r^n(\underline{x})$ is implicit, it is referred to as $\mathbb{B}_r(\underline{x})$ for simplicity. $\diamond$

The characteristic length (or hard-body radius) of agent i, $l_i \in (0, \infty)$, is defined as

$$l_i \doteq \sup_{\underline{x} \in B_i} \| \underline{x} - \mathbf{r}_i \| \tag{3}$$

where $B_i \subseteq \mathbb{R}^{d_{\mathbf{R}}}$ is the set of all points in the body of agent i, and where $\sup(\cdot)$ denotes the supremum operator. In this work, the B_i is approximated as the ball with radius l_i centered at the ith center of mass, i.e. $B_i = \mathbb{B}_{l_i}^{d_{\mathbf{R}}}(\mathbf{r}_i)$; this is referred to as the hard-body radius (HBR) assumption, and it is illustrated in Figure 1.
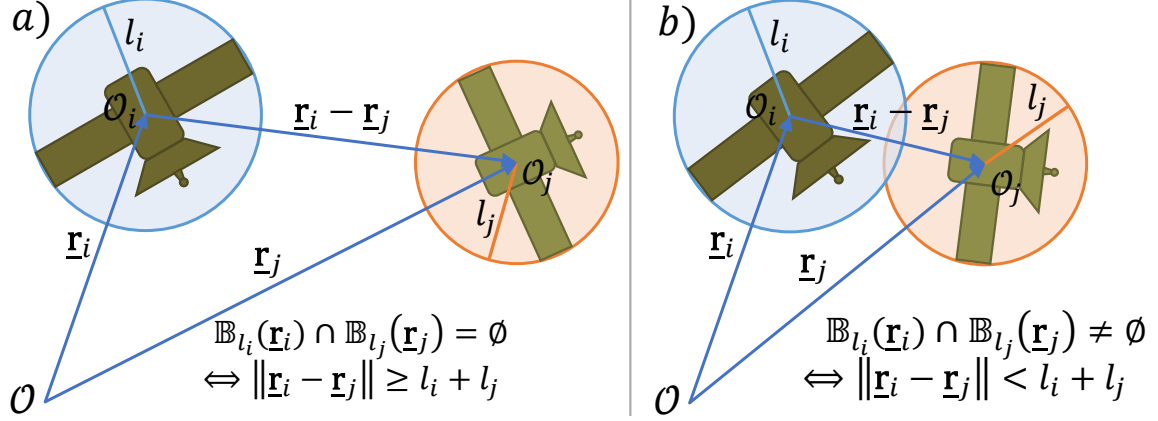
Figure 1: Agents under the HBR simplification: a) not colliding, and b) colliding. Note: these circles represent $d_{\mathbf{R}}$-balls that circumscribe agent bodies, not position pdf's.[12, 13, 21]

Let i and j refer to two agents in proximity. Through the HBR simplification, l_i represents a no-contact zone, i.e. agent i does not collide with any other agent j $(i \neq j)$ if no point belonging to the body of agent j becomes closer to the ith center of mass than a distance l_i. Thus, in order to avoid a collision with agent i, it is sufficient for agent j to be at least a distance l_i away from agent i, and vice versa. Using this intuition, the i-j collision event is formally defined as the condition given by

$$\mathbb{B}_{l_i}(\mathbf{r}_i) \cap \mathbb{B}_{l_j}(\mathbf{r}_j) \neq \emptyset \tag{4}$$

Whenever the condition in Eq. 4 holds, the distance between the respective centers of mass is less than the sum of their respective hard-body radii, as seen in Figure 1. Letting $l_{i,j} \doteq l_i + l_j$ denote the i-j joint hard-body radius, an equivalent collision condition is given by

$$\| \mathbf{r}_i - \mathbf{r}_j \| < l_{i,j} \tag{5}$$

When the exact positions of agents i and j are known, Eqns. 4 and 5 list Boolean conditions from which it can be ascertained, deterministically, whether such agents are colliding. In practice, however, because agent positions must be estimated, it is not possible to know them precisely. Therefore, whether a collision is occurring can only be established in a probabilistic sense. Nonetheless, the equivalent collision conditions listed in Eqns. 4 and 5 are employed in defining the probability measure in relative position space that corresponds to a collision event.

Definition 2 (Kinematic probability of collision). The kinematic probability of collision of agents i and j at time t, denoted by $\mathrm{KPC}_{i,j}(t)$, is defined as the probability of "the event that agents i and j are colliding at time t". Assuming the HBR simplification holds, then, $\mathrm{KPC}_{i,j}(t)$ can be expressed as

$$\mathrm{KPC}_{i,j}(t) = p\left(\| \mathbf{R}_{i,j}(t) \| < l_{i,j} \right) \tag{6}$$

Assuming that $\underline{\mathbf{R}}_{i,j}(t)$ is absolutely continuous, the probability measure in Eq. 6 can be computed as an integral of the pdf of $\underline{\mathbf{R}}_{i,j}(t)$, i.e. as given by

$$\mathrm{KPC}_{i,j}(t) = \int_{\underline{\mathbf{r}} \in V_{i,j}} \mathrm{pdf}_{\underline{\mathbf{R}}_{i,j}(t)}(\underline{\mathbf{r}}) \, d\underline{\mathbf{r}} \tag{7}$$

where the i-j intersection volume, denoted by $V_{i,j}$, is defined as the set

$$V_{i,j} \doteq \mathbb{B}_{l_{i,j}}^{d_{\mathbf{R}}}\left(\underline{\mathbf{0}}_{d_{\mathbf{R}} \times 1}\right) = \left\{\underline{\mathbf{r}} \in \mathbb{R}^{d_{\mathbf{R}}} : \|\underline{\mathbf{r}}\| < l_{i,j}\right\} \tag{8}$$

and where $\underline{\mathbf{0}}_{n \times 1}$ denotes the zero-valued vector in $\mathbb{R}^n$. $\qquad\qquad\qquad\qquad\qquad\qquad\quad \diamond$

Definition 2 is illustrated with two-dimensional example where the relative position is normally distributed, as shown in Figure 2, where the d-contours represent contours of constant Mahalanobis distance.[21]
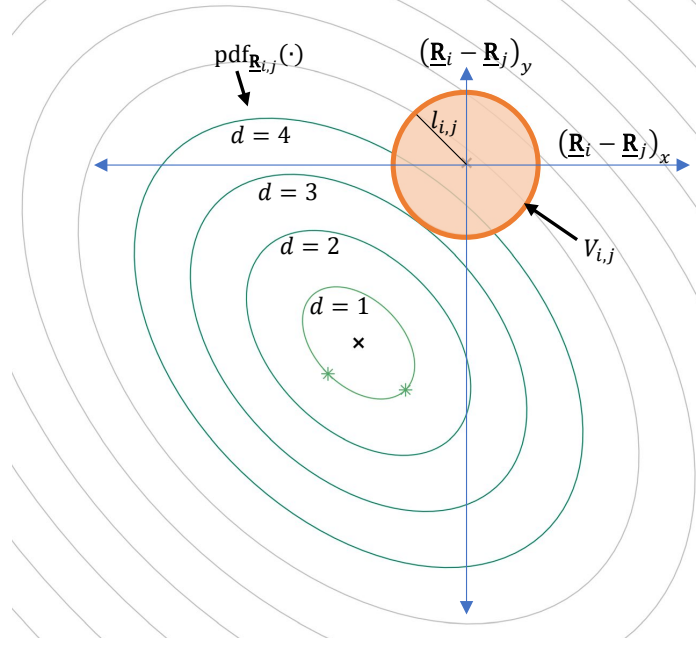
Figure 2: Conceptual KPC computation through integration of relative position pdf for a system with normally distributed (two-dimensional) relative position.

CW dynamics and geometry

In this work, it is assumed that simulation cases obey Clohessy Wiltshire (CW) relative orbital dynamics. The position of the deputy k about the chief c_0 ($[\underline{\mathbf{r}}_{k,c_0}]_H \in \mathbb{R}^3$, or simply $[\underline{\mathbf{r}}_k]_H$) is expressed in the coordinates of the Hill frame,[24] which is a rotating reference frame, and which is also designated as the RIC,[30] RTN,[31] and LVLH frame.[5] The CW relative dynamic state $[\underline{\mathbf{x}}_k]_H$ is completed by the relative position rate, i.e. $[\underline{\mathbf{x}}_k]_H^T = \left[[\underline{\mathbf{r}}_k]_H^T, [\underline{\dot{\mathbf{r}}}_k]_H^T\right]$. A CW dynamic system displays linear, time-invariant (LTI) dynamics. Hence, if the initial relative state is known at some time t_0, the relative state $[\underline{\mathbf{x}}_k]_H(t)$ may be computed as

$$[\underline{\mathbf{x}}_k]_H(t) = \Phi_{c_0}(t, t_0) [\underline{\mathbf{x}}_k]_H(t_0) \tag{9}$$

where Φ_{c_0} is the c_0 state transition matrix (STM), given by

$$\Phi_{c_0}(t, t_0) = \begin{bmatrix} 4 - 3c & 0 & 0 & \frac{s}{n_{c_0}} & \frac{2}{n_{c_0}} - \frac{2c}{n_{c_0}} & 0 \\ -6n_{c_0}(t - t_0) + 6s & 1 & 0 & -\frac{2}{n_{c_0}} + \frac{2c}{n_{c_0}} & \frac{4s}{n_{c_0}} - 3(t - t_0) & 0 \\ 0 & 0 & c & 0 & 0 & \frac{s}{n_{c_0}} \\ 3n_{c_0}s & 0 & 0 & c & 2s & 0 \\ -6n_{c_0} + 6n_{c_0}c & 0 & 0 & -2s & -3 + 4c & 0 \\ 0 & 0 & -n_{c_0}s & 0 & 0 & c \end{bmatrix} \tag{10}$$

where n_{c_0} refers to the mean periodic orbital motion of agent c_0 (in angular rate units), and where $c = \cos(n_{c_0}(t - t_0))$ and $s = \sin(n_{c_0}(t - t_0))$. Furthermore, if the CW trajectory of agent k about agent c_0 is

closed, i.e. if the relative trajectory is bounded (that is, there are no relative position terms that grow without bound), then the initial relative CW state $[\underline{\mathbf{x}}_k]_H (t_0)$ is constrained such that

$$[\dot{y}_k]_H (t_0) = -2n_{c_0} [x_k]_H (t_0) \tag{11}$$

Closed relative CW trajectories can be described in terms of the geometric parameters A_0, B_0, y_{off}, α_0 and β_0 as given by Equations 12, 13 and 14, in accordance with the notation of Schaub, et al.[5]

$$[x]_H (t) = A_0 \cos(n_{c_0}(t - t_0) + \alpha_0) \tag{12}$$

$$[y]_H (t) = -2A_0 \sin(n_{c_0}(t - t_0) + \alpha_0) + y_{\text{off}} \tag{13}$$

$$[z]_H (t) = B_0 \cos(n_{c_0}(t - t_0) + \beta_0) \tag{14}$$

It should be noted that these are five, not six, geometric parameters, owing to the closed CW trajectory constraint, given by Eq. 11, and they can be interpreted as follows:

- A_0: amplitude of $[x]_H$ motion.
- y_{off}: steady-state offset of $[y]_H$ motion. Note: the amplitude of $[y]_H$ motion about y_{off} is $2A_0$.
- B_0: amplitude of $[z]_H$ motion.
- α_0: phase angle of $[x]_H$ motion. Note: the $[y]_H$ motion leads the $[x]_H$ motion by a phase difference of $\pi/2$, i.e. by 0.25 chief orbit periods, regardless of the value of α_0. Thus, the $[x]_H$-$[y]_H$ motion is always a 1:2 ellipse centered at $(0, y_{\text{off}})$.
- β_0: phase angle of $[z]_H$ motion.

The α_0 and β_0 angles are only meaningful if the A_0 and B_0 amplitudes, respectively, are nontrivial. If defined, the $\beta_0 - \alpha_0$ geometric parameter creates the greatest variability in the shape of closed CW trajectories. In particular, the following cases are noteworthy:

- $\mathrm{mod}(\beta_0 - \alpha_0, 2\pi) \in \{0, \pi\}$. Here, the $[x]_H$ and $[z]_H$ motions are in phase and are either correlated or anti-correlated straight lines, whereas the $[y]_H$ and $[z]_H$ motions are out of phase, creating a $2:(B_0/A_0)$ ellipse. For example, in this $\beta_0 - \alpha_0$ case, if $B_0 = 2A_0$, then the relative trajectory as perceived in the $[y]_H$-$[z]_H$ plane is a 1:1 ellipse (i.e. a circle) centered at $(y_{\text{off}}, 0)$.
- $\mathrm{mod}(\beta_0 - \alpha_0, 2\pi) \in \{\pi/2, 3\pi/2\}$. Here, the $[y]_H$ and $[z]_H$ motions are in phase and are either correlated or anti-correlated straight lines, whereas the $[x]_H$ and $[z]_H$ motions are out of phase, creating a $1:(B_0/A_0)$ ellipse.
- $\mathrm{mod}(\beta_0 - \alpha_0, \pi/2) \neq 0$. Here, the $[z]_H$ motion is neither in phase nor out of phase with either the $[x]_H$ or $[y]_H$ motions, creating either correlated or anti-correlated ellipses in the $[x]_H$-$[z]_H$ and $[y]_H$-$[z]_H$ planes.

THEORY

Throughout the remainder of this work, for simplicity, the relative state $\underline{\mathbf{X}}_{i,j}$ and relative position $\underline{\mathbf{R}}_{i,j}$ are denoted as $\underline{\mathbf{X}}$ and $\underline{\mathbf{R}}$, respectively. Furthermore, only three-dimensional (3D) relative positions are considered.

Introducing radial probability measures

Radial probability measures – definition. This work draws heavily on the concept of radial probability measures of the relative position $\underline{\mathbf{R}}$; that is, in measures $h : [0, \infty) \to [0, 1]$ of the form

$$h(\rho) = p(\underline{\mathbf{R}} \in V_\rho) \tag{15}$$

where, for $\rho \geq 0$,

$$V_\rho \doteq \{\underline{\mathbf{r}} \in \mathbb{R}^3 : \|\underline{\mathbf{r}}\| \leq \rho\} = \mathbb{B}^3_\rho(\mathbf{0}_{3\times 1}) \cup \mathbb{S}^2_\rho(\mathbf{0}_{3\times 1}) \tag{16}$$

Because the relative position random variable $\underline{\mathbf{R}}$ is assumed to be absolutely continuous, the measure h can be computed as the integral

$$h(\rho) = \int_{\underline{\mathbf{r}} \in V_\rho} \mathrm{pdf}_{\underline{\mathbf{R}}}(\underline{\mathbf{r}})\, d\underline{\mathbf{r}} \tag{17}$$

where $\mathrm{pdf}_{\underline{\mathbf{R}}}(\cdot)$ exists a.e. and is non-negative where defined.

Because the set $\mathbb{S}_\rho^2(\underline{\mathbf{0}}_{3 \times 1}) = \{\underline{\mathbf{r}} \in \mathbb{R}^3 : \|\underline{\mathbf{r}}\| = \rho\}$ has zero measure in $\mathbb{R}^3$, it follows that

$$h(\rho) = \int_{\|\underline{\mathbf{r}}\| \leq \rho} \mathrm{pdf}_{\underline{\mathbf{R}}}(\underline{\mathbf{r}})\, d\underline{\mathbf{r}} = \int_{\|\underline{\mathbf{r}}\| < \rho} \mathrm{pdf}_{\underline{\mathbf{R}}}(\underline{\mathbf{r}})\, d\underline{\mathbf{r}} \tag{18}$$

Therefore, by definition, $\mathrm{KPC}_{i,j}$ is simply the radial probability measure of $\underline{\mathbf{R}}$ evaluated at the joint hard-body radius $l_{i,j}$. That is,

$$h(l_{i,j}) = \int_{\|\underline{\mathbf{r}}\| < l_{i,j}} \mathrm{pdf}_{\underline{\mathbf{R}}}(\underline{\mathbf{r}})\, d\underline{\mathbf{r}} =: \mathrm{KPC}_{i,j} \tag{19}$$

Norm of the relative position – definition. The norm of the relative position, or R, is defined as $R \doteq \|\underline{\mathbf{R}}\| = (\underline{\mathbf{R}}^T \underline{\mathbf{R}})^{1/2}$. Thus, R can be understood as the true inter-agent distance, which, due to uncertainty, cannot be known exactly.

Proposition 3. Let $\underline{X}$ be an absolutely continuous random variable in $\mathbb{R}^n$. Define $X \doteq \|\underline{X}\| = (\underline{X}^T \underline{X})^{1/2}$. Then, X is an absolutely continuous random variable as well. $\diamondsuit$

Proof. Omitted due to paper length limitation. $\square$

Because $\underline{\mathbf{R}}$ is assumed to be absolutely continuous, via Proposition 3, it follows that R is absolutely continuous. Therefore, pdf_R exists a.e., and cdf_R is an absolutely continuous function. Furthermore, h is an absolutely continuous function as well, which can be seeing by noting that

$$h(\rho) = p(\|\underline{\mathbf{R}}\| \leq \rho) = p(R \leq \rho) =: \mathrm{cdf}_R(\rho) \tag{20}$$

If $\mathrm{pdf}_{\underline{\mathbf{R}}}$ is known, $h(r)$ for $r \geq 0$ can be computed as

$$h(r) = \int_0^r \int_0^{2\pi} \int_0^\pi \mathrm{pdf}_{\underline{\mathbf{R}}}(\underline{\mathbf{r}}(\rho, \theta, \phi))\, \rho^2 \sin\phi\, d\phi\, d\theta\, d\rho \tag{21}$$

where $\underline{\mathbf{r}}(\rho, \theta, \phi)$ is a traditional spherical coordinate representation of $\underline{\mathbf{r}}$ as given by

$$\underline{\mathbf{r}}^T(\rho, \theta, \phi) = \rho \begin{bmatrix} \cos\theta \sin\phi & \sin\theta \sin\phi & \cos\phi \end{bmatrix} \tag{22}$$

where $\rho \geq 0$, $0 \leq \theta < 2\pi$, and $0 \leq \phi \leq \pi$. It follows that $\mathrm{pdf}_R(r)$ can be computed as an integral of $\mathrm{pdf}_{\underline{\mathbf{R}}}$ as given by

$$\mathrm{pdf}_R(r) = \left.\frac{dh(\rho)}{d\rho}\right|_{\rho=r} = r^2 \int_0^{2\pi} \int_0^\pi \mathrm{pdf}_{\underline{\mathbf{R}}}(\underline{\mathbf{r}}(r, \theta, \phi)) \sin\phi\, d\phi\, d\theta \tag{23}$$

Alternatively, the Lambert area-preserving mapping between the unit square and the unit 2-sphere, denoted by $T : [0, 1) \times [0, 1] \to \mathbb{S}^2$ as given by

$$T\left(\begin{bmatrix} y_1 \\ y_2 \end{bmatrix}\right) = \begin{bmatrix} \sqrt{1 - (1 - 2y_2)^2} \cos(2\pi y_1) \\ \sqrt{1 - (1 - 2y_2)^2} \sin(2\pi y_1) \\ 1 - 2y_2 \end{bmatrix}, \quad \begin{bmatrix} y_1 \\ y_2 \end{bmatrix} \in [0, 1) \times [0, 1] \tag{24}$$

7

may be used to create a spherical coordinate representation of $\underline{\mathbf{r}}$.[32] Using the Lambert transform, the computation of $h(r)$ becomes

$$h(r) = 4\pi \int_0^r \int_0^1 \int_0^1 \text{pdf}_{\underline{\mathbf{R}}}\left(\underline{\mathbf{r}}(\rho, y_1, y_2)\right) \rho^2 \, dy_2 \, dy_1 \, d\rho \tag{25}$$

and the computation of $\text{pdf}_R(r)$ becomes

$$\text{pdf}_R(r) = 4\pi r^2 \int_0^1 \int_0^1 \text{pdf}_{\underline{\mathbf{R}}}\left(\underline{\mathbf{r}}(r, y_1, y_2)\right) \, dy_2 \, dy_1 \tag{26}$$

where $\rho \geq 0$, $0 \leq y_1 < 1$, and $0 \leq y_2 \leq 1$, and where $\underline{\mathbf{r}}(\rho, y_1, y_2) = \rho \, T\left([y_1, y_2]^T\right)$.

The spherical coordinate-based integral methods presented in this subsubsection for computing radial probability measures (in Eqns. 21 and 25) and the pdf of R (in Eqns. 23 and 26) are not only intuitive, but also general in the sense that they are applicable regardless of the distribution of $\underline{\mathbf{R}}$ – as long as its pdf is accessible and well-defined.

Radial probability measures for non-singular, normal relative position

Within this subsection, let $\underline{\mathbf{R}}$ have a non-singular, multivariate normal distribution (MVN), i.e. $\underline{\mathbf{R}} \sim \mathcal{N}(\underline{\mu}, \Sigma)$, where $\underline{\mu} \in \mathbb{R}^3$, $\Sigma \in \mathbb{R}^{3\times3}$, $\Sigma > 0$, where the notation "> 0" implies that such is a symmetric, positive definite matrix. Then, for $\underline{\mathbf{r}} \in \mathbb{R}^3$, $\text{pdf}_{\underline{\mathbf{R}}}(\underline{\mathbf{r}})$ is given by

$$\text{pdf}_{\underline{\mathbf{R}}}(\underline{\mathbf{r}}) = \left((2\pi)^3 \det \Sigma\right)^{-1/2} \exp\left[-\frac{1}{2}(\underline{\mathbf{r}} - \underline{\mu})^T \Sigma^{-1}(\underline{\mathbf{r}} - \underline{\mu})\right] \tag{27}$$

Norm of non-singular, normal relative position – integral computation. When $\underline{\mathbf{R}}$ is non-singular normal, computing $h(r)$ and $\text{pdf}_R(r)$ in terms of traditional spherical coordinates can be accomplished by modifying Eqns. 21 and 23 into

$$h(r) = \int_0^r \int_0^{2\pi} \int_0^\pi g_1(\rho, \theta, \phi) \, d\phi \, d\theta \, d\rho \tag{28}$$

and

$$\text{pdf}_R(r) = \int_0^{2\pi} \int_0^\pi g_1(r, \theta, \phi) \, d\phi \, d\theta \tag{29}$$

where $\underline{\mathbf{r}}(\rho, \theta, \phi)$ is as given by Eq. 22, and where

$$g_1(\rho, \theta, \phi) = \left[\frac{\det(\Sigma^{-1})}{(2\pi)^3}\right]^{1/2} \exp\left[-\frac{1}{2}(\underline{\mathbf{r}}(\rho, \theta, \phi) - \underline{\mu})^T \Sigma^{-1}(\underline{\mathbf{r}}(\rho, \theta, \phi) - \underline{\mu})\right] \rho^2 \sin\phi \tag{30}$$

Similarly, $h(r)$ and $\text{pdf}_R(r)$ can be computed in terms of Lambert equal-area spherical coordinates by adjusting Eqns. 25 and 26 as given by

$$h(r) = \int_0^r \int_0^1 \int_0^1 g_2(\rho, y_1, y_2) \, dy_2 \, dy_1 \, d\rho \tag{31}$$

and

$$\text{pdf}_R(r) = \int_0^1 \int_0^1 g_2(r, y_1, y_2) \, dy_2 \, dy_1 \tag{32}$$

where $\underline{\mathbf{r}}(\rho, y_1, y_2) = \rho \, T\left([y_1, y_2]^T\right)$, and where

$$g_2(\rho, y_1, y_2) = \left[\frac{2}{\pi} \det(\Sigma^{-1})\right]^{1/2} \exp\left[-\frac{1}{2}(\underline{\mathbf{r}}(\rho, y_1, y_2) - \underline{\mu})^T \Sigma^{-1}(\underline{\mathbf{r}}(\rho, y_1, y_2) - \underline{\mu})\right] \rho^2 \tag{33}$$

Radial probability measures – approximations

Radial probability measures – Monte Carlo integration. An integral I of a function $f : \Omega \to \mathbb{R}$ of a random variable $\underline{\mathbf{X}}$ over its sample space $\Omega \subseteq \mathbb{R}^d$ can be understood as the expectation of $f(\underline{\mathbf{X}})$; that is,

$$I[f] = \int_{\underline{\mathbf{x}} \in \Omega} f(\underline{\mathbf{x}}) \, \mathrm{pdf}_{\underline{\mathbf{X}}}(\underline{\mathbf{x}}) \, d\underline{\mathbf{x}} =: \mathbb{E}[f(\underline{\mathbf{X}})] \tag{34}$$

assuming that $\mathrm{pdf}_{\underline{\mathbf{X}}}(\cdot)$ exists. If $\{\underline{\mathbf{x}}_k\}_{k \in \{1,\ldots,N\}}$ is a statistically random sample of $\underline{\mathbf{X}}$ with sample size $N \in \mathbb{N}$ (that is, the elements of the sample are independent and identically distributed (i.i.d.), with the same distribution as $\underline{\mathbf{X}}$), then $I[f]$ can be approximated through the expectation estimator given by[33]

$$\widehat{I}_N[f] = \frac{1}{N} \sum_{k=1}^{N} f(\underline{\mathbf{x}}_k) \tag{35}$$

This technique is the most simple version of Monte Carlo-based integration, and it has the following advantages.[34] First, through application of the expectation operator to Eq. 35, and noting that $\mathbb{E}[f(\underline{\mathbf{x}}_k)] = \mathbb{E}[f(\underline{\mathbf{X}})]$ for all $k \in \{1,\ldots,N\}$, it follows that $\mathbb{E}\left[\widehat{I}_N[f]\right] = I[f]$. Consequently, via the strong law of large numbers, $\widehat{I}_N[f]$ converges to $I[f]$ almost surely,[35] i.e. $p\left(\widehat{I}_N[f] \to I[f]\right) = 1$,[36] or

$$p\left(\lim_{N \to \infty} \widehat{I}_N[f] = I[f]\right) = 1 \tag{36}$$

Second, through the Central Limit Theorem (CLT), it can be shown that for large N, the approximation error magnitude $\left|I[f] - \widehat{I}_N[f]\right|$ is proportional to $N^{-1/2}$ (assuming an unbiased estimator), so increasing sample size generally improves the accuracy of the approximated integral.[33] Although this convergence rate is very slow, it does remain as $\mathcal{O}(N^{-1/2})$ regardless of the dimension of elements in a Monte Carlo sample; hence, Monte Carlo integration is a consistently viable tool for approximating integrals in high-dimensional spaces. The Monte Carlo (MC) estimator presented in Eq. 35 is crude or naïve because it does not implement variance reduction techniques such as importance sampling, antithetic variates or control variates.[35,37]

A crude MC estimator $\widehat{h}_N(\cdot)$ for the radial probability measure $h(\cdot)$ is given by

$$\widehat{h}_N(r) = \frac{1}{N} \sum_{k=1}^{N} f_{h,r}(\underline{\mathbf{r}}_k) \tag{37}$$

where $\{\underline{\mathbf{r}}_k\}_{k \in \{1,\ldots,N\}}$ is a Monte Carlo sample of $\underline{\mathbf{R}}$, and where $f_{h,r} : \mathbb{R}^3 \to \{0,1\}$ is an indicator function,[36] which is based on the definition of radial probability measures, and thus satisfies

$$f_{h,r}(\underline{\mathbf{r}}) = \begin{cases} 1, & \|\underline{\mathbf{r}}\| \leq r \\ 0, & \text{otherwise} \end{cases} \tag{38}$$

for $\underline{\mathbf{r}}$ in $\mathbb{R}^3$ and $r > 0$.

Characterizing the 99.73% minimum distance ($\rho_{3\sigma}$)

99.73% minimum distance ($\rho_{3\sigma}$) – definition. Let the constant $p_{3\sigma}$ be defined as

$$p_{3\sigma} \doteq 1 - \mathrm{cdf}_{\chi_1^2}(3^2) \approx 1 - 0.9973 = 0.0027 \tag{39}$$

As previously noted, the 99.73% minimum distance, or $\rho_{3\sigma}$, is the distance away from the origin so that $100(1 - p_{3\sigma})$ percent of relative position cases have Euclidean distances from the origin that are greater than $\rho_{3\sigma}$. In other words, $\rho_{3\sigma}$ can be defined as

$$\rho_{3\sigma} \doteq \min\{r \in [0, \infty) : \mathrm{cdf}_R(r) = p_{3\sigma}\} \tag{40}$$

It will be shown $\rho_{3\sigma}$ is a quantile of the distribution of R.

Definition 4 (Quantiles and quantile function[38, 39]). Take $p \in (0, 1)$. For a univariate, real-valued RV X with cdf denoted by F_X, a quantile $x \in \mathbb{R}$ of order p of the distribution of X satisfies $F_X(x) \geq p$ and

$$p\,(X < x) = \lim_{\varepsilon \to 0^+} F_X(x - \varepsilon) \leq p \tag{41}$$

The quantile function of X, $F_X^{-1} : (0, 1) \to \mathbb{R}$ is a generalized inverse of F_X, i.e. it satisfies $F_X^{-1}(p) \doteq \inf S_p$, where $S_p = \{x \in \mathbb{R} : F_X(x) \geq p\}$, where $\inf(\cdot)$ denotes the infimum operator. Since cdfs are right continuous, S_p is closed on the left, i.e. $\inf S_p \in S_p$.[27] Therefore, $F_X^{-1}(p)$ is given by

$$F_X^{-1}(p) = \min \{x \in \mathbb{R} : F_X(x) \geq p\} \tag{42}$$

and it exists for $p \in (0, 1)$. Therefore, $F_X^{-1}(p)$ is the minimum quantile of order p of the distribution of X.

If X is continuous, its cdf is continuous, so it has no jump discontinuities. In this case, $F_X^{-1}(p)$ is given by

$$F_X^{-1}(p) = \min \{x \in \mathbb{R} : F_X(x) = p\} \tag{43}$$

Finally, if F_X is strictly increasing, then F_X^{-1} is the true inverse of F_X. $\diamond$

In the context of real-valued random variables, absolutely continuous RVs (i.e. RVs that have pdfs) are also continuous RVs (i.e. RVs with continuous cdfs), although the converse is not true (see the Cantor function, a classical counterexample: it has a continuous cdf, as well as a zero a.e. derivative; hence, the cdf is not equal to the integral of its derivative).[27] Since R is absolutely continuous (per the assumption of absolute continuity of **R**, and via Proposition 3), cdf_R is a continuous function by implication. Therefore, via Definition 4, $\rho_{3\sigma}$ is the minimum $p_{3\sigma}$-quantile of R; furthermore, $\rho_{3\sigma}$ exists and is unique.

It should be noted that there may be $p_{3\sigma}$-quantiles of R other than $\rho_{3\sigma}$. For example, it is possible that $\mathrm{pdf}_R(r) = 0$ a.e. for $r \in (\rho_{3\sigma}, \rho_{3\sigma} + \varepsilon)$ for some $\varepsilon > 0$; in that case, for any such r, $\mathrm{cdf}_R(r) = p_{3\sigma}$. However, it is useful to define $\rho_{3\sigma} = \mathrm{cdf}_R^{-1}(p_{3\sigma})$ because, as an output of the quantile function, $\rho_{3\sigma}$ is the smallest $p_{3\sigma}$-quantile of R, which is consistent with its interpretation as a collision risk boundary. Additionally, if cdf_R is strictly increasing in the neighborhood of $p_{3\sigma}$, then $\rho_{3\sigma}$ is the unique $p_{3\sigma}$-quantile of R.

99.73% minimum distance ($\rho_{3\sigma}$) – sensitivity analysis. For a univariate random variable X, the derivative of the quantile function of X is given by

$$\frac{d}{dy}\mathrm{cdf}_X^{-1}(y)\Big|_{y=u} = \lim_{\varepsilon \to 0} \frac{\mathrm{cdf}_X^{-1}(u + \varepsilon) - \mathrm{cdf}_X^{-1}(u)}{\varepsilon} \tag{44}$$

for $0 < u < 1$. When X is absolutely continuous (i.e. when its pdf exists; see the Notation subsection), Parzen has shown that the derivative of the quantile function of X satisfies the relation

$$\mathrm{pdf}_X\left(\mathrm{cdf}_X^{-1}(u)\right)\left[\frac{d}{dy}\mathrm{cdf}_X^{-1}(y)\Big|_{y=u}\right] = 1 \tag{45}$$

for $0 < u < 1$.[39] When applied to R, and noting that $\rho_{3\sigma}$ satisfies $\mathrm{cdf}_R^{-1}(p_{3\sigma}) = \rho_{3\sigma}$, it follows that

$$\frac{d}{dy}\mathrm{cdf}_R^{-1}(y)\Big|_{y=p_{3\sigma}} = \frac{1}{\mathrm{pdf}_R(\rho_{3\sigma})} \tag{46}$$

Since $\rho_{3\sigma} = \mathrm{cdf}_R^{-1}(p_{3\sigma}) = \rho_{3\sigma}(p_{3\sigma})$, the derivative of quantile function of R evaluated at $p_{3\sigma}$ can be interpreted as the derivative of $\rho_{3\sigma}$ with respect to its target probability, $p_{3\sigma}$. Therefore,

$$\frac{d\rho_{3\sigma}}{dp_{3\sigma}} = \frac{1}{\mathrm{pdf}_R(\rho_{3\sigma})} \tag{47}$$

Hence, the effects on $\rho_{3\sigma}$ caused by small changes in $p_{3\sigma}$ may be quantified via Eq. 47.

It should be noted that this sensitivity analysis could be extended to apply to cases where $\mathrm{pdf}_R(\rho_{3\sigma})$ is undefined. One example of this is when $\mathrm{pdf}_R(\rho_{3\sigma}^-)$ and $\mathrm{pdf}_R(\rho_{3\sigma}^+)$ both exist and are finite, yet do not share the same value; in this case, the derivative of cdf_R evaluated at $\rho_{3\sigma}$ (i.e. $\mathrm{pdf}_R(\rho_{3\sigma})$) does not exist. Another example is when $\mathrm{pdf}_R(\rho_{3\sigma}^+) = 0$; in this case, there are multiple $p_{3\sigma}$-quantiles of R, and $\rho_{3\sigma}$ is the smallest one. Since any $\rho < \rho_{3\sigma}$ satisfies $h(\rho) < p_{3\sigma}$, it follows that $\mathrm{cdf}_R(\rho)$ is strictly increasing for ρ that approaches $\rho_{3\sigma}$ from the left. Therefore, $\mathrm{pdf}_R(\rho_{3\sigma}^-) > 0$, which also implies that $\mathrm{pdf}_R(\rho_{3\sigma})$ does not exist.

In both of the aforementioned examples, the sensitivity analysis could be carried out by replacing $\mathrm{pdf}_R(\rho_{3\sigma})$ in Eq. 47 with $\mathrm{pdf}_R(\rho_{3\sigma}^-)$ instead, given that it is not only well defined, but because it carries the same interpretation as $\mathrm{pdf}_R(\rho_{3\sigma})$, i.e. how much $p_{3\sigma}$ would be reduced with a small reduction in $\rho_{3\sigma}$. Clearly, when $h(\rho)$ is strictly increasing in the neighborhood of $\rho_{3\sigma}$, it follows that $\mathrm{pdf}_R(\rho_{3\sigma})$ exists and is equal to $\mathrm{pdf}_R(\rho_{3\sigma}^-)$, so $\mathrm{pdf}_R(\rho_{3\sigma}^-)$ could be used without loss of generality.

METHODOLOGY

99.73% minimum distance ($\rho_{3\sigma}$) – numerical computation methodology

The approach undertaken here for the numerical computation of $\rho_{3\sigma}$ is through nested numerical solution of ordinary differential equations (ODEs), as seen though the combination of Figures 3 and 4. This is accomplished by using MATLAB's `ode113` function, which is an ODE solver best suited for high accuracy numerical solution of non-stiff ODEs.[40]
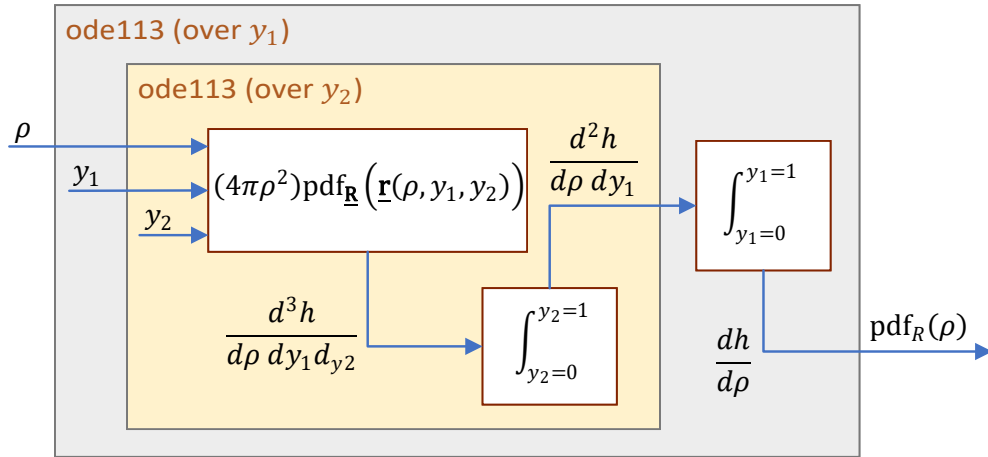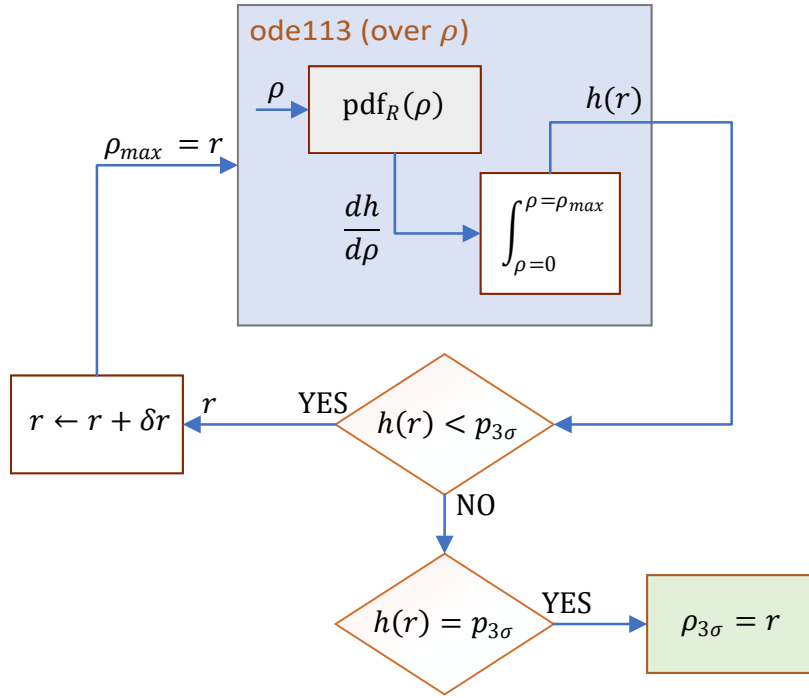

Figure 3: Numerical computation of the pdf of the norm of the relative position using nested implementation of the `ode113` solver.

The notation of the `ode113` function, as well as for the other MATLAB ODE solvers, assumes that the variables to be integrated have computable time derivatives, and that it is the desire of the user to solve for the time histories of such variables over a closed interval of time. In the present paradigm, however, instead of integrating with respect to time, use of the `ode113` solver is adapted in order to integrate a function with respect to degrees of freedom that represent spatial coordinates.

It should be noted that y_1 and y_2 are the coordinates of the Lambert equal-area unit square parametrization of the unit 2-sphere. Then, as shown in Fig. 3, for a given $\rho \in (0, \infty)$, $\mathrm{pdf}_R(\rho) = dh/d\rho$ is computed through `ode113` as the integral of $d^2h/d\rho\, dy_1$ over the sample space of Y_1 (i.e. $[0, 1)$), which, in turn, is computed through `ode113` as the integral of $d^3h/d\rho\, dy_1 dy_2$ over the sample space of Y_2 (i.e. $[0, 1]$).

By definition, the definite integral of $\mathrm{pdf}_R(\cdot)$ over the interval $[0, r]$ for $r \geq 0$ is the radial probability measure $h(r)$. Hence, $\rho_{3\sigma}$ can be interpreted as the solution of the constrained optimization problem

$$\rho_{3\sigma} = \min_{r \in (0,\infty)} r \tag{48}$$

Figure 4: Numerical computation of radial probability measures and the 99.73% minimum distance ($\rho_{3\sigma}$) using nested implementation of the `ode113` solver.

where $r \in (0, \infty)$ is subject to the integral equation constraint given by

$$p_{3\sigma} = \int_0^r \mathrm{pdf}_R(\rho)d\rho =: h(r) \tag{49}$$

However, because $h(\cdot)$ is non-decreasing, numerical computation of $\rho_{3\sigma}$ can be accomplished as follows. First, a small value of $r \in (0, \infty)$ is chosen, and $h(r)$ is computed. Second, if $h(r) < p_{3\sigma}$, then r is increased until $h(r^*) = p_{3\sigma}$, as posed in Eq. 49. When this condition is first met, the value of r^* will also satisfy the condition posed in Eq. 48; consequently, $\rho_{3\sigma} = r^*$ in this case. Hence, optimization is avoided by using the non-decreasing property of $h(\cdot)$.

The foregoing methodology for the numerical computation of $\rho_{3\sigma}$ is implemented in the `ode113` solver (integrating over ρ coordinates, as seen in Fig. 4) through use of the `events` setting, which employs root-finding in order to check for one or multiple univariate equality constraints. In this case, the `events` setting is used to approximately identify the first r^* such that $h(r^*) - p_{3\sigma} = 0$, and integration is stopped when this condition is first met. Overall, there are three levels of `ode113`-based numerical integration: the highest level (i.e. in ρ), the mid level (i.e. in y_1), and the lowest level (i.e. in y_2); additionally, the logic for solving for $\rho_{3\sigma}$ is implemented at the ρ-level.

99.73% minimum distance ($\rho_{3\sigma}$) – sample computation methodology

Given the statistical guarantees of crude MC estimators as previously discussed, such estimators may be used to construct approximations to univariate probability distributions via the empirical cdf; in turn, the empirical cdf may be used to formulate quantile estimators.[35] Therefore, Monte Carlo sampling is chosen for validating the foregoing `ode113`-based approach for numerical computation of $\rho_{3\sigma}$.

The methodology is illustrated in Fig. 5, and it begins by drawing a Monte Carlo of the relative position between two agents, **R**, based on instantaneous statistics of the distribution. Subsequently, the norm of each element in the sample is computed, which induces a MC sample of R; this sample is then sorted, which yields
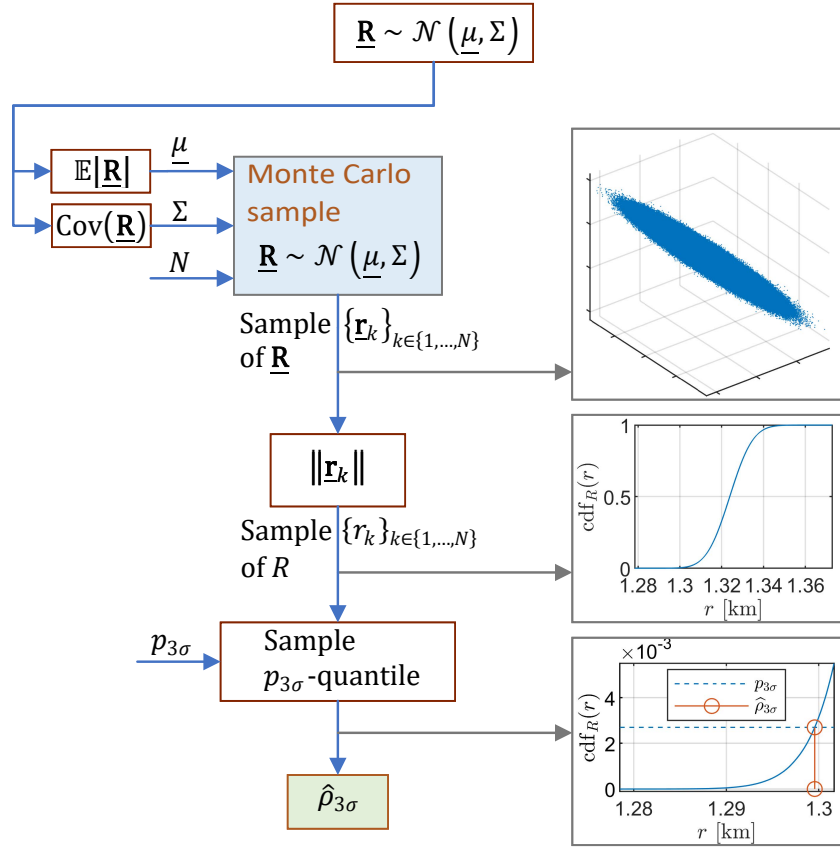
Figure 5: Sample computation of the 99.73% minimum distance ($\rho_{3\sigma}$) through Monte Carlo simulation based on instantaneous relative position statistics.

the order statistics of the sample of R, i.e. $r_{(1)} \leq \cdots \leq r_{(N)}$, where N is the sample size. Then, $\widehat{\rho}_{3\sigma}$ is obtained through a linear interpolation estimator,[38] which is described as follows:

1. Compute $k = \lfloor (N-1)p_{3\sigma} + 1 \rfloor$, where $\lfloor \cdot \rfloor$ is the floor operator.

2. Compute $\tau = ((N-1)p_{3\sigma} + 1) - k$.

3. Obtain $\widehat{\rho}_{3\sigma}$ as given by

$$\widehat{\rho}_{3\sigma} = (1-\tau)r_{(k)} + (\tau)r_{(k+1)} \tag{50}$$

In MATLAB, this sample quantile estimator is implemented through the `prctile` function.[41] It should be noted that, even though the notation of Fig. 5 assumes that the relative position has a multivariate normal distribution (whose samples can be drawn in MATLAB using the `mvnrnd` function[41]), the general process of quantile computation presented herein is applicable to Monte Carlo samples drawn from any absolutely continuous relative position distribution.

99.73% minimum distance ($\rho_{3\sigma}$) – derivative computation methodology

As previously stated, this work aims to investigate the regularity of $\rho_{3\sigma}$, i.e. whether small changes of the defining parameter of $\rho_{3\sigma}$ (namely, $p_{3\sigma}$) result in commensurately small changes to $\rho_{3\sigma}$ itself. Such effective changes to $p_{3\sigma}$ would naturally arise from numerical errors in checking whether $h(\rho_{3\sigma}) = p_{3\sigma}$. In particular, with some given initial uncertainty description, if such regularity were exhibited over extended time horizons, this would be helpful for the purposes of predicting the risk of future collisions via $\rho_{3\sigma}$, as it would give

validity to $\rho_{3\sigma}$ over propagated horizons. Since the formulation of $\rho_{3\sigma}$ is instantaneous (i.e. it depends on the uncertainty at a single time t only), ascertaining $\rho_{3\sigma}(t)$ regularity over extended horizons entails the following basic steps: propagating relative state statistics to a given time, extracting relative position information, computing $\rho_{3\sigma}$, performing regularity calculations, and then repeating the process at a subsequent time.

The `ode113`-based $\rho_{3\sigma}$ computation methodology was developed so as to directly mimic the iterated integral formulation of $h(\cdot)$ listed in Eq. 25, which itself follows directly from its definition through a coordinate transformation; hence, this methodology allows for estimates of $\rho_{3\sigma}$ that conceptually retain its interpretation. However, it is not feasible to implement this methodology accurately in practice over extended time horizons. For example, with a ρ-level step size of 1 m, and a $\rho_{3\sigma}$ of 1 km, the total spatial volume increase with each step size in the vicinity of $\rho_{3\sigma}$ is 1.26×10^7 times larger than $1\,\mathrm{m}^3$. Thus, unless the pdf of $\underline{\mathbf{R}}$ has zero mean and is spherically symmetric, capturing probability masses in such radial shells accurately requires increasingly small angular step sizes (in y_1 and y_2). The likelihood of round-off errors introduced to the computation, as well as the general computational expense, are exacerbated when increasingly small step sizes are needed for an acceptable resolution in $\rho_{3\sigma}$ itself – especially if, after extended horizons, uncertainty diverges in some (but not all) directions (which does occur in CW dynamics with MVN prior distribution). However, in order to quantify the sensitivity of $\rho_{3\sigma}$ to small changes in $p_{3\sigma}$, which can be accomplished via $d\rho_{3\sigma}/dp_{3\sigma}$, Eq. 47 implies that $\rho_{3\sigma}$ must be first calculated, and then $\mathrm{pdf}_R\left(\rho_{3\sigma}\right)$ must be evaluated.

Therefore, in this work, a hybrid approach is adopted for estimating $d\rho_{3\sigma}/dp_{3\sigma}$. First, $\rho_{3\sigma}$ is approximated through the crude MC estimator $\widehat{\rho}_{3\sigma}$ as shown in Fig. 5; the validity of this assumption is explored in the Results and Discussion section. Second, the pdf of R is evaluated at $\widehat{\rho}_{3\sigma}$ using the `ode113`-based approach shown in Fig. 3. Finally, $d\rho_{3\sigma}/dp_{3\sigma}$ is approximated as

$$\frac{d\rho_{3\sigma}}{dp_{3\sigma}} \approx \frac{1}{\mathrm{pdf}_R\left(\widehat{\rho}_{3\sigma}\right)} \tag{51}$$

RESULTS AND DISCUSSION

Simulation parameters and CW dynamic cases

As mentioned previously, dynamic cases in this work are assumed to be subject to CW dynamics. Furthermore, it is assumed that the distribution of the initial relative state $\underline{\mathbf{X}}(t_0)$ is multivariate, non-degenerate normal (MVN); that is, the pdf of $\underline{\mathbf{X}}(t_0)$ is given by

$$\mathrm{pdf}_{\underline{\mathbf{X}}(t_0)}\left(\mathbf{x}\right) = \left((2\pi)^6 \det \Sigma_{\underline{\mathbf{X}}}(t_0)\right)^{-1/2} \exp\left[-\frac{1}{2}\left(\mathbf{x}-\bar{\mathbf{X}}(t_0)\right)^T \left[\Sigma_{\underline{\mathbf{X}}}(t_0)\right]^{-1}\left(\mathbf{x}-\bar{\mathbf{X}}(t_0)\right)\right] \tag{52}$$

for $\mathbf{x} \in \mathbb{R}^6$, where $\bar{\mathbf{X}}(t_0) = \mathbb{E}\left[\underline{\mathbf{X}}(t_0)\right]$ and where $\Sigma_{\underline{\mathbf{X}}}(t_0) > 0$ are the expected value (or mean) and covariance, respectively, of the initial relative state $\underline{\mathbf{X}}(t_0)$. This is denoted as $\underline{\mathbf{X}}(t_0) \sim \mathcal{N}\left(\bar{\mathbf{X}}(t_0), \Sigma_{\underline{\mathbf{X}}}(t_0)\right)$.

Because CW dynamics are linear, the distribution of the relative state remains multivariate, non-degenerate normal; that is, $\underline{\mathbf{X}}(t) \sim \mathcal{N}\left(\bar{\mathbf{X}}(t), \Sigma_{\underline{\mathbf{X}}}(t)\right)$, where $\bar{\mathbf{X}}(t)$ and $\Sigma_{\underline{\mathbf{X}}}(t)$ are analytically propagated, as given by

$$\bar{\mathbf{X}}(t) = \Phi\left(t, t_0\right)\bar{\mathbf{X}}(t_0) \tag{53}$$

$$\Sigma_{\underline{\mathbf{X}}}(t) = \Phi(t, t_0)\left[\Sigma_{\underline{\mathbf{X}}}(t_0)\right]\Phi^T(t, t_0) \tag{54}$$

where $\Phi\left(t, t_0\right)$ is the CW STM listed in Eq. 10. The initial expected relative state $\bar{\mathbf{X}}(t_0)$ is prescribed in terms of the geometric parametrization of a closed CW relative orbit as depicted in the Background section, and these parameters are listed in Table 1. Hence, the expected value of the distribution follows a closed CW trajectory, even though the covariance matrix may grow without bound over time.

For simplicity, the initial relative state covariance is assumed to be diagonal, i.e. as given by

$$\Sigma_{\underline{\mathbf{X}}}\left(t_0\right) = \mathrm{diag}\left(\begin{bmatrix} \sigma^2_{[x]_H}(t_0) & \sigma^2_{[y]_H}(t_0) & \sigma^2_{[z]_H}(t_0) & \sigma^2_{[\dot{x}]_H}(t_0) & \sigma^2_{[\dot{y}]_H}(t_0) & \sigma^2_{[\dot{z}]_H}(t_0) \end{bmatrix}\right) \tag{55}$$

14

Table 1: Initial relative state expectation parameters

Cases	Comments	$\bar{A}_0$	$\bar{B}_0$	$\bar{y}_{\text{off}}$	$\bar{\alpha}_0$	$\bar{\beta}_0 - \bar{\alpha}_0$
		[km]			[deg]	
3D.001	No $[z]_H$ motion	1	0	0	0	N/A
3D.002	With $[z]_H$ motion ($[x]_H$ and $[z]_H$ motion in phase)	1	0.1	0	0	0
3D.c ($c \in \{003, 004, \ldots, 026\}$)	With $[z]_H$ motion ($[x]_H$ and $[z]_H$ motion out of phase)	1	0.1	0	$15(c-3)$ ($\alpha_0 \in \{0, 15, \ldots, 345\}$)	90

Table 2: Initial relative state covariance parameters

Parameter at t_0	$\sigma_{[x]_H}$	$\sigma_{[y]_H}$	$\sigma_{[z]_H}$	$\sigma_{[\dot{x}]_H}$	$\sigma_{[\dot{y}]_H}$	$\sigma_{[\dot{z}]_H}$
Value	10 m	5 m	0.5 m	0.25 m/s	0.75 m/s	0.05 m/s

where its components are listed in Table 2.

The semimajor axis of the orbit of the chief agent is assumed as $\bar{a} = 6800$ km; hence, its mean motion $\bar{n}$ may be computed in terms of Earth's standard gravitational parameter μ_E as $\bar{n} \doteq \sqrt{\mu_E/\bar{a}^3}$, where $\mu_E = 3.986004418 \times 10^5$ km^3/s^2. The simulation horizon is two orbit periods of the chief agent, and the timestep resolution is 3.8754 seconds, which corresponds to 1/1440$^{\text{th}}$ of one orbit period, or 1/4$^{\text{th}}$ of one degree (of mean anomaly) of one revolution of the orbit of the chief spacecraft.

This particular choice of orbit altitude, and of initial relative state expectation and covariance parameters, are driven by previous work, which suggests that, for those specific parameters, $\rho_{3\sigma}$ and the KPC (for a joint hard-body radius $l_{i,j}$ of 32 m) are related to each other in a way that is consistent with intuition.[12,13] That is, over a horizon of two orbit periods, $\rho_{3\sigma}$ indicates smallest separation while the KPC indicates highest collision risk, and the $\rho_{3\sigma}$ indicates largest separation while the KPC indicates lowest collision risk; this is not observed with other separation indicators studied. Hence, such parameters are used in order to validate the foregoing interpretation of $\rho_{3\sigma}$ as a true probabilistic risk boundary in relative position space.

Finally, the Monte Carlo sample size is chosen as 3.2×10^8 particles. For an MVN distribution, it is conjectured that such a sample size should be able to capture the probability of significant events where the significance threshold is set at 10^{-7}.[12,13] Under this assumption, this sample size affords agreement of the $p_{3\sigma}$-quantile of R to within approximately 4.4 significant digits in $p_{3\sigma}$.

99.73% minimum distance ($\rho_{3\sigma}$) – sample validation results

The first result in this work, summarized in Figs. 6 and 7, demonstrates the agreement between numerical and sample approaches to the computation of $\rho_{3\sigma}$. Even though this is only corroborated for Example 3D.001, these results are representative of other examples as well because of their shared methodology.

For Example 3D.001, Fig. 6 shows that the numerical and sample $\rho_{3\sigma}$ waveforms agree to within 9.15 cm over 0.0729 chief orbit periods (or 6.78 minutes, which corresponds to 106 timesteps). At worst, the discrepancies observed represent no more than 0.0098% difference relative to the computed magnitude of $\rho_{3\sigma}$. Therefore, to within low discrepancy, the numerical and sample $\rho_{3\sigma}$ waveforms converge to each other over the restricted horizon $[0, t_c]$, where t_c denotes the cutoff propagation time for the numerical $\rho_{3\sigma}$ waveform. This kind of agreement is adequate for the computation of $\rho_{3\sigma}$ sensitivity, as effects on $d\rho_{3\sigma}/dp_{3\sigma}$ (from errors in $\rho_{3\sigma}$) are proportional to the derivative of pdf_R (i.e. a second derivative of probabilities in R, which is a higher order effect). It remains to be ascertained whether $\rho_{3\sigma}$ itself is estimated sufficiently accurately.

Letting $C_b([0, 2P])$ denote the space of continuous and bounded functions (under the sup-norm) in $[0, 2P]$, where P denotes the chief orbit period, Figure 7 shows that $\widehat{\rho}_{3\sigma} \in C_b([0, 2P])$. Since both numerical and sample approaches can be made arbitrarily accurate, it is possible to create sequences of $\rho_{3\sigma}$ waveform estimators that are Cauchy (i.e. sequences whose elements become arbitrarily close to one another). Since

$C_b\left([0, 2P]\right)$ is a complete function space (i.e. a space in which Cauchy sequences converge to an element of said space),[29] the numerical and sample $\rho_{3\sigma}$ waveforms each converge to an element of $C_b\left([0, 2P]\right)$, and since both methods converge to each other, it follows that both methods converge to the same function $f \in C_b\left([0, 2P]\right)$ (which could be interpreted as the true $\rho_{3\sigma}$ waveform) – at least when limiting the domain to $[0, t_c]$. Within this restricted horizon, this establishes that the sample approach is representative of the numerical approach (so the former is an acceptable substitute for the latter), and that the sample approach converges to the true $\rho_{3\sigma}$. Given the general MC convergence guarantees aforementioned, it is concluded that the sample methodology is an acceptable estimator for $\rho_{3\sigma}$ over the full horizon $[0, 2P]$.
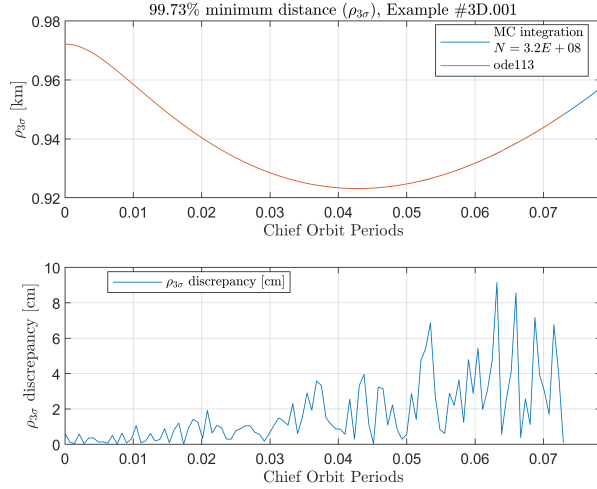
Figure 6: Example 3D.001, $\rho_{3\sigma}$ waveform results: (upper) numerical and sample results; (lower) absolute difference between numerical and sample results.
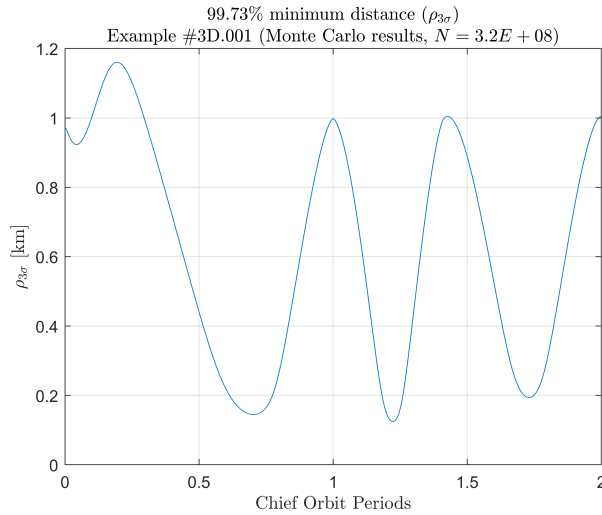

Figure 7: Example 3D.001, sample $\rho_{3\sigma}$ waveform results over full horizon.

99.73% minimum distance ($\rho_{3\sigma}$) – sensitivity analysis results

For Example 3D.001, Figure 8 shows the time history of the derivative of $\rho_{3\sigma}$ with respect to its target probability $p_{3\sigma}$, $d\rho_{3\sigma}/dp_{3\sigma}$ (in units of [km/probability unit]), as approximated via Eq. 51, i.e. as computed via the hybrid numerical/sample approach described in the Methodology section. For this example, it is found that $d\rho_{3\sigma}/dp_{3\sigma}$ is continuous over time. Let $\delta p = 0.01\%$. If the target probability $p_{3\sigma}$ were to change by

as much as δp (which would be a significant change since $\delta p / p_{3\sigma} \approx 3.7\%$), a first order estimate of the corresponding change in $d\rho_{3\sigma}$, $\delta\rho_{3\sigma}$, would yield that $\delta\rho_{3\sigma} = 5.1$ m at worst over $[0, 2P]$. This is a small change compared to $\rho_{3\sigma}$, considering that $\rho_{3\sigma}$ is in the order of hundreds to thousands of meters over $[0, 2P]$.
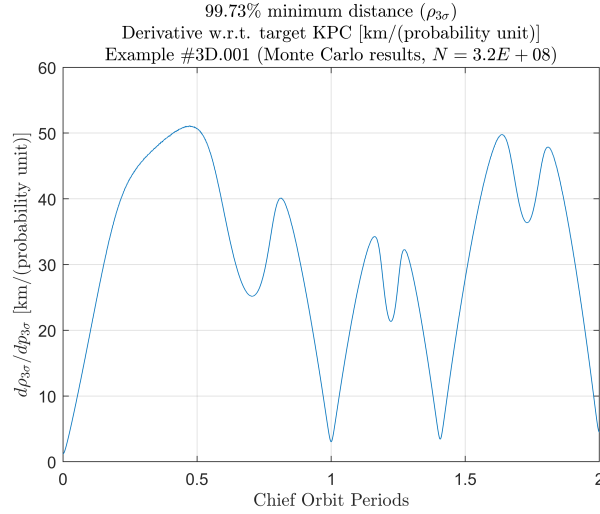

Figure 8: Example 3D.001, derivative of $\rho_{3\sigma}$ with respect to its target probability $p_{3\sigma}$, $d\rho_{3\sigma}/dp_{3\sigma}$, full horizon time-history.

For Example 3D.001, Figure 9 shows the first order approximation of the relative sensitivity of $\rho_{3\sigma}$ to a change δp in $p_{3\sigma}$; that is, it shows $\delta\rho_{3\sigma}/\rho_{3\sigma}$. For this example, it is found that a relative change in target probability of 3.7% causes, at worst, a change in $\rho_{3\sigma}$ of up to 1.88%. This shows that, within the confines of Example 3D.001, $\rho_{3\sigma}$ exhibits regularity, i.e. small changes in $p_{3\sigma}$ also result in small changes to $\rho_{3\sigma}$. The regularity of $\rho_{3\sigma}$ is observed more generally in other relative orbit regimes. As displayed in Figure 10, given a 3.7% variation in $p_{3\sigma}$, the maximum relative change in $\rho_{3\sigma}$ is less than 1.9% for relative orbits with no cross-track motion (Example 3D.001), with along-track and cross-track motion in phase (Example 3D.002), and with along-track and cross-track motion out of phase (Examples 3D.003–026).
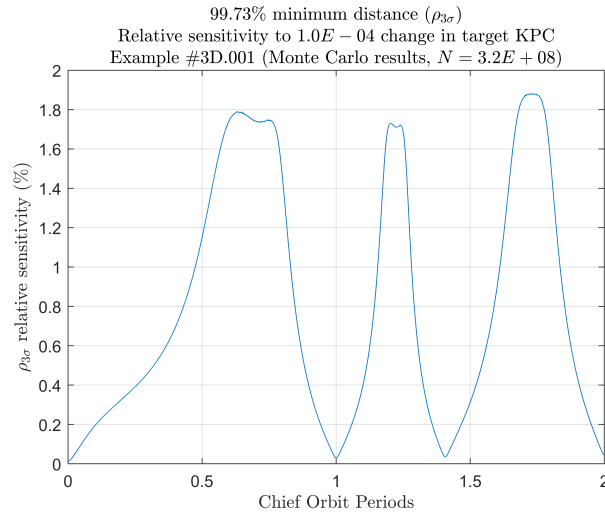
Figure 9: Example 3D.001, relative sensitivity of $\rho_{3\sigma}$ to a change $\delta p = 0.01\%$ in target probability $p_{3\sigma}$

Whether these relative (and actual) sensitivities are acceptable depends on the specific operational scenario at hand. For example, for a minimum $\rho_{3\sigma}$ of 125 m, in a scenario where the tolerance for instantaneous
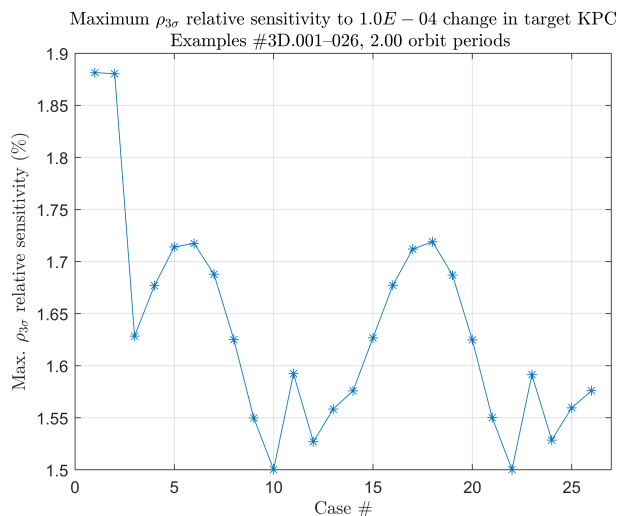
Figure 10: Examples 3D.001-026, maximum relative sensitivity of $\rho_{3\sigma}$ to a change $\delta p = 0.01\%$ in target probability $p_{3\sigma}$.

collision risk is $p_{3\sigma}$ and the inter-spacecraft keep-out distance (i.e. joint HBR) is 50 m, a 5.1 m error in the $\rho_{3\sigma}$ estimate would not be problematic, but it would be for a keep-out distance of 120 m. Rather, these results imply that, to within commensurate tolerances, it is valid to interpret $\rho_{3\sigma}$ as a probabilistic risk boundary in the first place, with the understanding that errors in its computation must be accounted for in practice.

These results demonstrate that, for the dynamic examples considered in this work, that $\rho_{3\sigma}$ is regular with respect to $p_{3\sigma}$, i.e. small changes in $p_{3\sigma}$ cause small changes in $\rho_{3\sigma}$. This validates the interpretation of $\rho_{3\sigma}$ as a probabilistic risk boundary in relative position space under the assumptions made (CW dynamics, and the specific relative state uncertainties chosen). Considering that the 1-σ error rms (in the relative position) grows to as much as over 25 km over the propagation horizon considered (for all cases, since they have the same relative state covariance), the regularity displayed by $\rho_{3\sigma}$ is especially noteworthy.

CONCLUSION

In this work, when the relative position between two objects is a random variable, the norm of the relative position is characterized as a univariate random variable in its own right. The 99.73% minimum distance, or $\rho_{3\sigma}$, is intepreted as the $p_{3\sigma}$-quantile of the distribution of the norm of relative position, where $p_{3\sigma}$ is a constant with approximate value of 0.27%. It has been proposed that $\rho_{3\sigma}$ should be interpreted as a probabilistic collision risk boundary in relative position space in the sense that, for actual keep-out zones smaller than $\rho_{3\sigma}$, the kinematic (or instantaneous) probability of collision (KPC) between two objects is less than $p_{3\sigma}$, and for keep-out zones larger than $\rho_{3\sigma}$, the KPC is less than $p_{3\sigma}$. Under the assumption of Clohessy-Wiltshire (CW) dynamics over several regimes of relative orbits in Low-Earth Orbit, it is found that $\rho_{3\sigma}$ exhibits regularity with respect to $p_{3\sigma}$. That is, small changes in $p_{3\sigma}$ produce changes in $\rho_{3\sigma}$ that are commensurately small as well. Therefore, under these assumptions, the regularity of $\rho_{3\sigma}$ validates the aforementioned interpretation of $p_{3\sigma}$ as a probabilistic collision risk boundary in relative position space.

These findings motivate further exploration of the $\rho_{3\sigma}$ construct. It would be helpful to establish whether $\rho_{3\sigma}$ exhibits similar regularity under different relative orbit representations (e.g. relative orbit elements), under different dynamic models (e.g. including higher order gravity effects, as well as atmospheric drag), and under different assumptions regarding the nature of the uncertainty (e.g. non-normality of relative state distributions). If $\rho_{3\sigma}$ exhibits regularity under more general conditions such as those listed, the foregoing interpretation of $\rho_{3\sigma}$ would also hold in such conditions, which would afford greater applicability to this construct. Additionally, utilizing $\rho_{3\sigma}$ as a constraint in chance-constrained optimal control problems should

be explored in the context of applications to spacecraft formation station-keeping and collision avoidance.

REFERENCES

[1] D. P. Scharf, F. Y. Hadaegh, and S. R. Ploen, "A survey of spacecraft formation flying guidance and control (part I): guidance," *Proceedings of the 2003 American Control Conference*, Vol. 2, Denver, CO, IEEE, Jun. 2003, pp. 1733–1739, 10.1109/ACC.2003.1239845.

[2] K. Alfriend, S. R. Vadali, P. Gurfil, J. How, and L. Breger, *Spacecraft Formation Flying: Dynamics, Control and Navigation*, ch. 1, 14, pp. 1–11, 329–330. Elsevier Astrodynamics Series, Oxford, UK: Butterworth–Heinemann (Elsevier Science), 2010.

[3] J. R. Wertz, "Mission Concept Definition and Exploration," *Space Mission Engineering: The New SMAD* (J. R. Wertz, D. F. Everett, and J. J. Puschell, eds.), Space Technology Library, ch. 4, pp. 61–82, Hawthorne, CA: Microcosm Press, 2011.

[4] S. J. Chung, S. Bandyopadhyay, R. Foust, G. P. Subramanian, and F. Hadaegh, "Review of Formation Flying and Constellation Missions Using Nanosatellites," *Journal of Spacecraft and Rockets*, Vol. 53, No. 3, 2016, pp. 567–578, 10.2514/1.A33291.

[5] H. Schaub and J. L. Junkins, "Spacecraft Formation Flying," *Analytical Mechanics of Space Systems*, ch. 14, pp. 593–673, Reston, VA: AIAA Education Series, 2nd ed., 2009, 10.2514/4.105210.

[6] B. Tapley, J. Ries, S. Bettadpur, D. Chambers, M. Cheng, F. Condi, B. Gunter, Z. Kang, P. Nagel, R. Pastor, T. Pekker, S. Poole, and F. Wang, "GGM02 – An improved Earth gravity field model from GRACE," *Journal of Geodesy*, Vol. 79, Nov. 2005, pp. 467–478, 10.1007/s00190-005-0480-z.

[7] A. K. Sugihara El Maghraby, A. Grubisic, C. Colombo, and A. Tatnall, "A novel approach to microwave interferometric radiometry in the geostationary orbit using formation flight," *67th International Astronautical Congress of the International Astronautical Federation*, Guadalajara, Mexico, Sep. 2016, pp. 1–14.

[8] A. W. Koenig, B. Macintosh, and S. D'Amico, "Formation Design of Distributed Telescopes in Earth Orbit for Astrophysics Applications," *Journal of Spacecraft and Rockets*, Vol. 56, No. 5, 2019, pp. 1462–1477, 10.2514/1.A34420.

[9] G. Wang and W. T. Ni, "Numerical simulation of time delay interferometry for eLISA/NGO," *Classical and Quantum Gravity*, Vol. 30, Feb. 2013, pp. 1–19, 10.1088/0264-9381/30/6/065011.

[10] G. L. Slater, S. M. Byram, and T. W. Williams, "Collision Avoidance for Satellites in Formation Flight," *Journal of Guidance, Control, and Dynamics*, Vol. 29, No. 5, 2006, pp. 1140–1146, 10.2514/1.16812.

[11] S. Hilton, R. Sabatini, A. Gardi, H. Ogawa, and P. Teofilatto, "Space traffic management: towards safe and unsegregated space transport operations," *Progress in Aerospace Sciences*, Vol. 105, Feb. 2019, pp. 98–125, 10.1016/j.paerosci.2018.10.006.

[12] U. E. Nunez Garzon and E. G. Lightsey, "Relating Collision Probability and Miss Distance Indicators in Spacecraft Formation Collision Risk Analysis," *2020 AAS/AIAA Astrodynamics Specialist Conference*, AAS 20-528, South Lake Tahoe, CA, Aug. 2020, pp. 1–20.

[13] U. E. Nunez Garzon and E. G. Lightsey, "Relating collision probability and separation indicators in spacecraft formation collision risk analysis," *Journal of Guidance, Control, and Dynamics*, Oct. 2020. Under review for publication.

[14] S. D'Amico and O. Montenbruck, "Proximity Operations of Formation-Flying Spacecraft Using an Eccentricity/Inclination Vector Separation," *Journal of Guidance, Control, and Dynamics*, Vol. 29, No. 3, 2006, pp. 554–563, 10.2514/1.15114.

[15] D. Morgan, S.-J. Chung, L. Blackmore, B. Acikmese, D. Bayard, and F. Y. Hadaegh, "Swarm-Keeping Strategies for Spacecraft Under J2 and Atmospheric Drag Perturbations," *Journal of Guidance, Control, and Dynamics*, Vol. 35, No. 5, 2012, pp. 1492–1506, 10.2514/1.55705.

[16] R. Opromolla, G. Fasano, G. Rufino, and M. Grassi, "Design of relative trajectories for in orbit proximity operations," *Acta Astronautica*, Vol. 145, Apr. 2018, pp. 342–356, 10.1016/j.actaastro.2018.01.062.

[17] A. Richards, T. Schouwenaars, J. P. How, and E. Feron, "Spacecraft Trajectory Planning with Avoidance Constraints Using Mixed-Integer Linear Programming," *Journal of Guidance, Control, and Dynamics*, Vol. 25, No. 4, 2002, pp. 755–764, 10.2514/2.4943.

[18] J. B. Mueller, P. R. Griesemer, and S. J. Thomas, "Avoidance Maneuver Planning Incorporating Station-Keeping Constraints and Automatic Relaxation," *Journal of Aerospace Information Systems*, Vol. 10, No. 6, 2013, pp. 306–322, 10.2514/1.54971.

[19] R. Bevilacqua, T. Lehmann, and M. Romano, "Development and experimentation of LQR/APF guidance and control for autonomous proximity maneuvers of multiple spacecraft," *Acta Astronautica*, Vol. 68, No. 7, 2011, pp. 1260–1275, 10.1016/j.actaastro.2010.08.012.

[20] Y. Wang, X. Chen, D. Ran, Y. Zhao, Y. Chen, and Y. Bai, "Spacecraft formation reconfiguration with multi-obstacle avoidance under navigation and control uncertainties using adaptive artificial potential function method," *Astrodynamics*, Vol. 4, Mar. 2020, pp. 41–56, 10.1007/s42064-019-0049-x.

[21] U. E. Nunez Garzon and E. G. Lightsey, "Mahalanobis Shell Sampling (MSS) Method for Collision Probability Computation," *AIAA SciTech 2021 Forum*, AIAA 2021-1855, Nashville, TN, AIAA, Jan. 2021, pp. 1–25.

[22] R. Serra, D. Arzelier, M. Joldes, and A. Rondepierre, "Probabilistic Collision Avoidance for Long-term Space Encounters via Risk Selection," *Advances in Aerospace Guidance, Navigation and Control: Third CEAS Specialist Conference on Guidance, Navigation and Control* (J. Bordeneuve-Guibé, A. Drouin, and C. Roos, eds.), Toulouse, France, Springer International Publishing, Apr. 2015, pp. 679–698, 10.1007/978-3-319-17518-8_39.

[23] J.-B. Caillau, M. Cerf, A. Sassi, E. Trélat, and H. Zidani, "Solving chance constrained optimal control problems in aerospace via kernel density estimation," *Optimal Control Applications and Methods*, Vol. 39, No. 5, 2018, pp. 1833–1858, 10.1002/oca.2445.

[24] G. W. Hill, "Researches in the Lunar Theory," *American Journal of Mathematics*, Vol. 1, No. 1, 1878, pp. 5–26, 10.2307/2369430.

[25] W. H. Clohessy and R. S. Wiltshire, "Terminal guidance system for satellite rendezvous," *Journal of Aerospace Sciences*, Vol. 27, No. 9, 1960, pp. 653–658, 10.2514/8.8704.

[26] H. Schwarzlander, "Part 4: Transformations and Multiple Random Variables," *Probability Concepts and Theory for Engineers*, ch. 4, pp. 227–304, John Wiley & Sons, Ltd., 2011, 10.1002/9781119990895.ch4.

[27] P. Billingsley, *Probability and measure*, ch. 1, 4, 6, pp. 158–198, 254–326, 400–481. Wiley Series in Probability and Mathematical Statistics, New York: John Wiley & Sons, Ltd., 3rd ed., 1995.

[28] J. G. Hocking and G. S. Young, "Topological Spaces and Functions," *Topology*, ch. 1, pp. 1–36, Reading, MA: Addison-Wesley, Inc., 1st ed., 1961.

[29] C. Heil, "Metric and Normed Spaces," *Introduction to Real Analysis*, Graduate Texts in Mathematics, ch. 1, pp. 15–32, Cham: Springer International Publishing, 2019, 10.1007/978-3-030-26903-6.

[30] A. Dietrich and J. W. McMahon, "Orbit Determination Using Flash Lidar Around Small Bodies," *Journal of Guidance, Control, and Dynamics*, Vol. 40, No. 3, 2017, pp. 650–665, 10.2514/1.G000615.

[31] J. Sullivan, S. Grimberg, and S. D'Amico, "Comprehensive Survey and Assessment of Spacecraft Relative Motion Dynamics Models," *Journal of Guidance, Control, and Dynamics*, Vol. 40, No. 8, 2017, pp. 1837–1859, 10.2514/1.G002309.

[32] J. S. Brauchart, J. Dick, and L. Fang, "Spatial low-discrepancy sequences, spherical cone discrepancy, and applications in financial modeling," *Journal of Computational and Applied Mathematics*, Vol. 286, Oct. Oct. 2015, pp. 28–53, 10.1016/j.cam.2015.02.023.

[33] R. E. Caflisch, "Monte Carlo and quasi-Monte Carlo methods," *Acta Numerica*, Vol. 7, 1998, p. 1–49, 10.1017/S0962492900002804.

[34] J. Dick, F. Y. Kuo, and I. H. Sloan, "High-dimensional integration: The quasi-Monte Carlo way," *Acta Numerica*, Vol. 22, 2013, p. 133–288, 10.1017/S0962492913000044.

[35] C. Lemieux, "The Monte Carlo Method," *Monte Carlo and Quasi-Monte Carlo Sampling*, ch. 1, pp. 1–39, New York, NY: Springer New York, 2009, 10.1007/978-0-387-78165-5.

[36] D. P. Kroese, T. Taimre, and Z. I. Botev, "Appendix A: Probability and Stochastic Processes," *Handbook of Monte Carlo Methods*, pp. 605–651, John Wiley & Sons, Ltd., 2011, 10.1002/9781118014967.app1.

[37] A. Genz and F. Bretz, "Methods That Approximate the Integral," *Computation of Multivariate Normal and t Probabilities*, ch. 4, pp. 29–54, Berlin, Heidelberg: Springer Berlin Heidelberg, 2009, 10.1007/978-3-642-01689-9.

[38] R. V. Hogg, J. W. McKean, and A. T. Craig, *Introduction to Mathematical Statistics*, ch. 1, 4, pp. 1–84, 255–320. Boston: Pearson, 8th ed., 2019.

[39] E. Parzen, "Nonparametric Statistical Data Modeling," *Journal of the American Statistical Association*, Vol. 74, No. 365, 1979, pp. 105–121, 10.2307/2286734.

[40] The MathWorks, Inc., "Ordinary Differential Equations (ODEs)," *MATLAB® Mathematics*, ch. 11, pp. 11–1 – 11–74, Natick, MA: The MathWorks, Inc., MATLAB R2019b ed., Sep. 2019.

[41] The MathWorks, Inc., *Statistics and Machine Learning Toolbox™ User's Guide*, ch. 3, 5, pp. 3–1 – 3–22, 5–1 – 5–196. Natick, MA: The MathWorks, Inc., MATLAB R2019b ed., Sep. 2019.